LA-UR-20-24032

Title:	Preshot Report for the NIF Discovery Science DDCyl Campaign: D_Hyd_DDCyl_DRT_DDD/EEE/FFF
Author(s):	Sauppe, Joshua Paul; Palaniyappan, Sasikumar; Tobias, Benjamin John; Kline, John L.; Flippo, Kirk Adler; Landen, O. L.; Shvarts, D.; Stalsberg, Krista Lynn; Batha, Steven H.; Bradley, Paul Andrew; Loomis, Eric Nicholas; Vazirani, Nomita Nirmal; Fiedler Kawaguchi, Codie Yoshiko; Kot, Lynn; Zylstra, Alex; Schmidt, Derek William; Day, Thomas H.
Intended for:	Report
Issued:	2020-06-02

Preshot Report for the NIF Discovery Science `DDCyl` Campaign: D_Hyd_DDCyl_DRT_DDD/EEE/FFF

Prepared by J. P. Sauppe[1], S. Palaniyappan[1], and B. Tobias[1]
on behalf of the Cylindrical Implosion Team

John Kline[1], Kirk Flippo[1], Nino Landen[2], Dov Shvarts[3],
Krista Stalsberg[1], Steven Batha[1], Paul Bradley[1], Eric Loomis[1], Nomita Vazirani[1],
Codie Fiedler-Kawaguchi[1], Lynn Kot[1], Alex Zylstra[2], Derek Schmidt[1], Tom Day[1]

[1]Los Alamos National Laboratory
[2]Lawrence Livermore National Laboratory
[3]Ben-Gurion University of the Negev

Scheduled for:
February 12, 2020
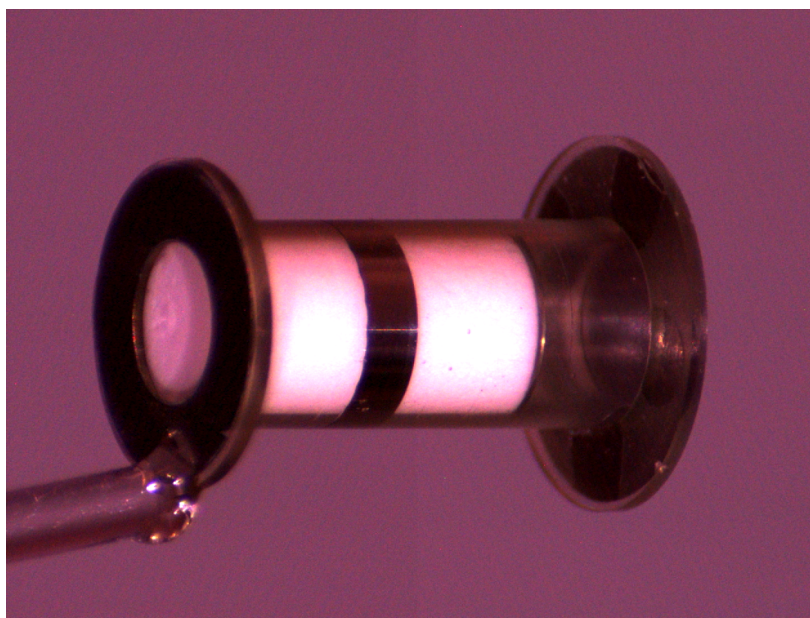
Contents

1 Introduction

The first Discovery Science shot day with the `NIF DDCyl` campaign demonstrated that Rayleigh-Taylor instability growth during the deceleration phase is scale-invariant for targets that varied in radial dimension and implosion time-scale by a factor of three. Smaller cylindrical implosions at the `OMEGA` laser facility were compared to the larger cylinders fielded in our first `NIF` outing. Both sets of targets had an initial $m = 20$ sinusoidal perturbation machined on the inner surface of an embedded aluminum marker layer, with the amplitude larger by the same factor of three for the `NIF`-scale targets. We observed growth factors of 14 at late time ($t/\lambda = 7.7$ ns, where $\lambda = 1$ for `OMEGA` and $\lambda = 3$ for `NIF`). These used a high density (300 mg/cm^3) CH foam core, providing a very long period of deceleration before the rebounding shock hit the incoming spike tips, but the final convergence was only CR≈ 2.25.

For our second shot day with this campaign, we are attempting to increase the convergence ratio to CR≥ 5 before reshock, while still measuring instability growth during the convergence/deceleration phase. As discussed in previous reports, the best way to increase convergence before reshock is to lower the density of the central foam. The preshot designs called for the use of a 30 mg/cm^3 CH foam, though the as-built foams are closer to 40–42 mg/cm^3, which is predicted to result in a final CR≈ 5.1 before reshock. Other than the lower foam density, the target design is identical to those used previously.

1.1 Laser Drive

The drive will remain the same as in the previous shot day (0.589 TW/beam in a 3 ns square pulse with a total of 226 kJ of laser energy). Although small increases can be eked out by increasing the power and/or energy of the pulse, this would also change our assumption of coupling efficiency of the laser energy to hydrodynamic motion of the target (as well as affect our optics damage usage). Recall that we use an *ad hoc* laser power multiplier, η_{laser}, since we are not currently using the cross-beam energy transfer (CBET) package in these `xRAGE` simulations. The pre-shot designs for our first shot day assumed $\eta_{\mathrm{laser}} \approx 0.8$, in-line with what we had found worked well for the `OMEGA`-scale targets. More accurate post-shot modeling indicates that the `NIF`-scale targets are better modeled with $\eta_{\mathrm{laser}} \approx 0.75$, likely due to the slightly higher initial illumination intensity on the target surface. Since we have a reasonably good understanding of how this drive couples to the target, we opted not to change it for this second shot day.

In the previous shot day, we used the BABLon7 (7 ns) backlighter pulse in order to capture a longer portion of the implosion trajectory for each target. However, to avoid optics damage issues, this limits the total power of the backlighter beams and thus the total intensity on the backlighter foil. For this shot day, we have opted to use the BABLon4 (4 ns) backlighter pulse. This allows us to increase the power on four of the eight backlighter beam quads to 1.4 TW/beam. The other four backlighter quads share amplifiers with the drive beams, so we have to drive them at reduced power (between 0.72 TW/beam and 0.86 TW/beam). The increased intensity on the backlighter foil will increase the x-ray conversion efficiency and help alleviate some of the poor signal-to-noise issues we observed in the previous shot day.

1.2 Target Types

As in our first shot day, we plan to field one smooth target and two perturbed targets. For the smooth target, we will attempt to image both before and after the shock hits the cylinder axis (nominally imaging 13.6–17.6 ns). The two perturbed targets will nominally have identical $m = 20$ initial perturbations, and we will image on either side of shock rebound (one will image 11.6–15.6 ns and the other will image 14.6–18.6 ns).

1.3 Objectives

The primary goal is to

- measure single-mode instability growth of a machined initial perturbation at CR≥ 4.

With the lower foam density, this growth should be dominated more by convergence (Bell-Plesset) effects rather than the deceleration of the interface (though that will still be present). The measured growth will be compared to predictions of our `xRAGE` simulations.

A secondary goal of the shot day is to

- improve the quality of the framing camera images obtained during the implosion.

The framing camera images obtained on the first shot day at the `NIF` suffered greatly from poor signal-to-noise. In addition to changing the backlighter pulse length, many other factors which could have contributed to the poor quality images were identified. In addition to the shortened backlighter pulse mentioned previously, we have made several additional changes in the diagnostic setup to compensate for this. These changes will be discussed in Sec. 4.

1.4 Shot Day Rules of Engagement

As in the first shot day, we want to prioritize the amount of data that we can collect. If a shot is canceled, it will NOT be rescheduled, so **our plan is to shoot the targets even if some of the beams need to be dropped.** `NIF` technicians have examined the as-built targets, and they believe that we will not need to drop any drive beams due to possible concerns over interfering with the target insertion stalk.

2 Target Metrology

The target design is nominally identical to the previous Discovery Science shot day. The dimensions of the assembled targets are listed in Table 1, along with the nominal design dimensions. The target dimensions were extracted from a spreadsheet provided by Tom Day containing information on each of the mandrels during the build process. Following the leaching process, the outer diameter of the epoxy ablator over the marker band (Ablator OR) is directly measured, as is the inner diameter of the epoxy tube at the axial end of the target (Ablator IR).

Based on my understanding, target fabrication includes a small shoulder on a portion of the mandrel and machines the sine-wave inside of that shoulder. The outer diameter of the shoulder is known, and the depth to the trough of the sine-wave is measured, providing information on the innermost radius of the aluminum marker (Pert. IR, in the table). The sine-wave amplitude is measured (Peak to Valley), and the initial bubble radius may be inferred (Pert. OR). After the machining phases, the outer diameter of the aluminum band is measured using the Keyence, giving the average outer radius of the marker (Marker Avg. OR). Foam densities were estimated using x-ray transmission through the samples, and foam diameters were measured by target fabrication.

Table 1: Dimensions of assembled `NIF` targets. Information extracted from "Mandrel Inspection" spreadsheet provided by Tom Day.

NIF Shot #	S11 (DDD)	S12 (EEE)	S13 (FFF)	
NIF Target #	M-M0_0_36-04	M-M20_12_36-05	M-M20_12_36-06	
Type	Smooth	Mode 20	Mode 20	Nominal
Inspection spreadsheet				
Spool #	Sm4	M20_02	M20_03	
Ablator OR [μm]	1465.8	1479.0	1478.25	1479
Ablator IR [μm]	1287.9	1269.65	1274.5	1290/1278
Marker Avg. OR [μm]	1325.00	1324.0	1321.5	1326
Marker Avg. IR [μm]	1290.70	1289.6	1290.35	1290
Avg. Thickness [μm]	34.30	34.40	31.15	36
Pert. OR [μm]		1301.7	1302.65	1302
Pert. IR [μm]		1277.5	1278.05	1278
Peak to Valley [μm]		24.2	24.6	24
Foam #	6	15	13	
Height [μm]	—	—	—	5000
Outer Radius [μm]	1286.0	1266.5	1272.0	1290/1278
DCS Dens. [mg/cc]	42.6	42.1	40.5	30
Touchprobe Data				
$m = 20$ Amp. [μm]		12.360	12.172	12

2.1 CT Scans

After leaching the mandrels but before final assembly, all of the spools were scanned using computerized tomography (CT scan). Tom Day mentioned that this CT data was likely not as constraining as that in the "Mandrel Inpsection" spreadsheet. Consequently, the CT data is not included at this time.

LA-UR-20-xxxxx

2.2 Touchprobe Measurements

For perturbed targets, a touchprobe is used to measure the perturbations machined on the outer surface of the mandrel before they are coated with aluminum. The touchprobe gives the height and depth as a function of angle, but the actual radial offset (from $r = 0$) is not able to be measured with this technique. Touchprobe measurements of the as-machined outer surface perturbation for the two perturbed target mandrels are shown in Fig. 1 along with the desired single-mode $m = 20$ perturbation at 12 μm initial amplitude (24 μm peak-to-valley). (Note that the touchprobe data has been filtered to remove $m \leq 7$ and $m \geq 100$ from this plot.) The touchprobe measurements reasonably approximate the desired single-mode initial condition, though the Fourier transform indicates the presence of higher harmonics ($m = 40$, $m = 60$, etc.) at modest amplitude. The amplitude of the primary mode is very close to the desired value, as can be seen in Table 1.
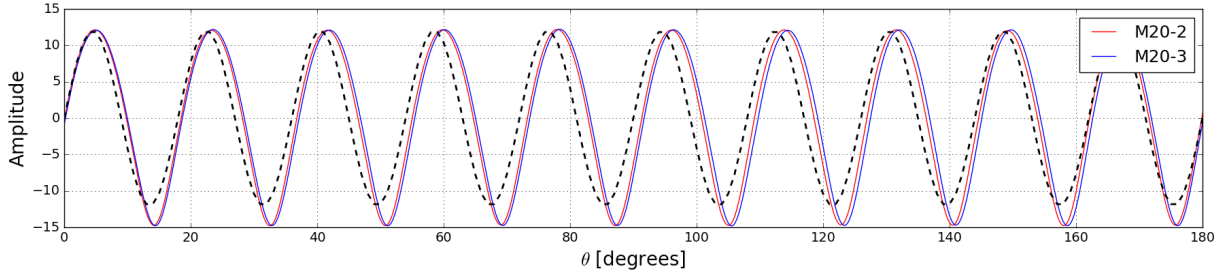

Figure 1: Touchprobe measurements showing the perturbation machined on the outer surface of the copper mandrel before being plated with aluminum.

3 Preshot Simulations

3.1 1D Simulations

On the previous shot day, we used a 300 mg/cm^3 central foam to provide a long period of deceleration phase Rayleigh-Taylor growth. This results in limited convergence of the marker, as can be seen in the left column of Fig. 2(a). The final convergence ratio is near CR=2.25 for this design. For the upcoming shot day, we plan to use a lower 40 mg/cm^3 foam. This should result in considerably more convergence before shock rebound, as shown in the right column of Fig. 2(a). The convergence ratio just before reshock here is CR=5.1. Note that the color scales differ considerably between the two plots.
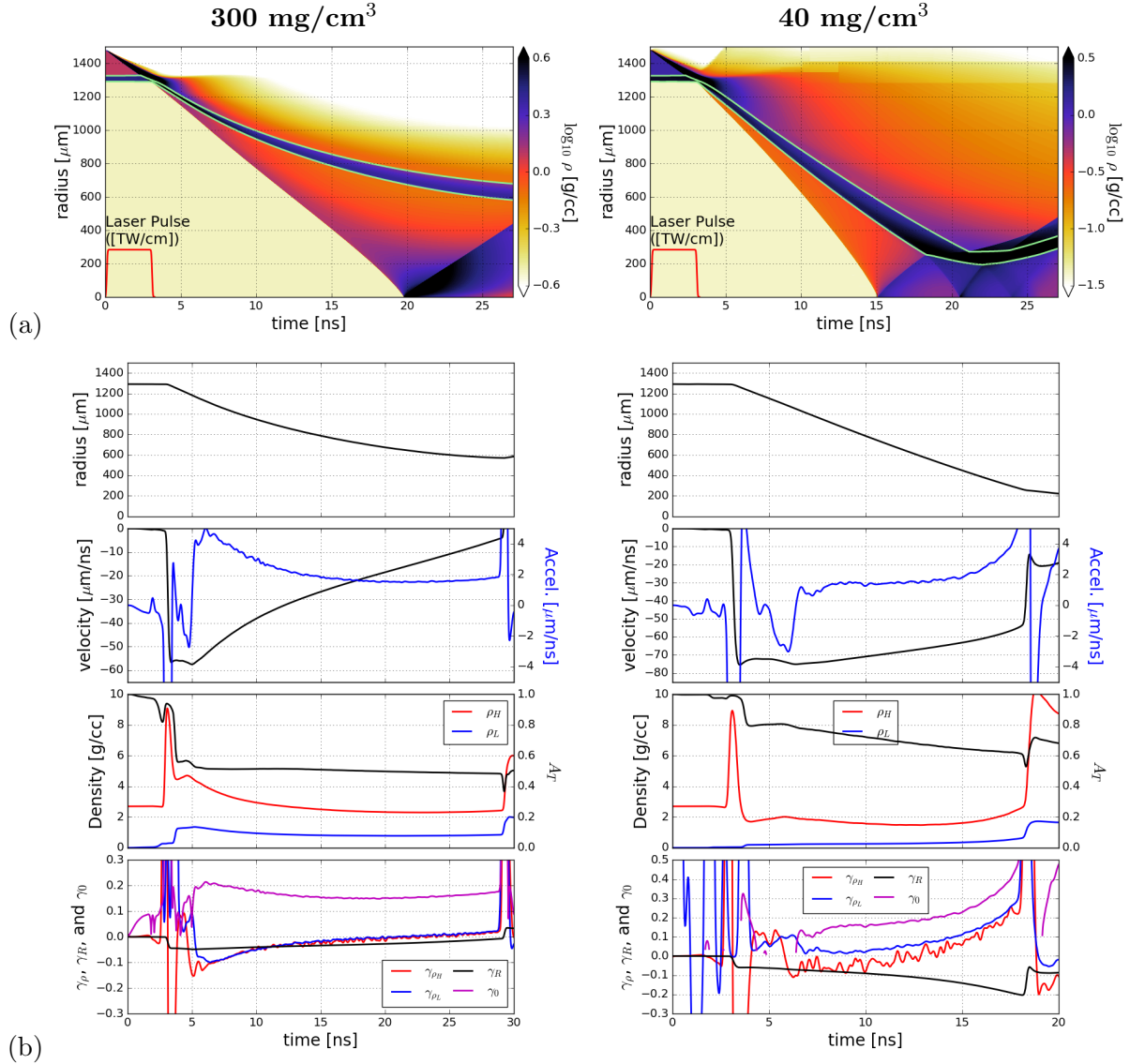
Figure 2: (a) Log density versus radius and time for nominal dimension target with 300 mg/cm^3 foam (left) and 40 mg/cm^3 foam (right). Note that color scales differ. (b) Interface position, velocity, and acceleration, along with density and Atwood number at the interface and terms from the linear evolution equation ($\gamma_0 = \sqrt{A_T m \ddot{r}/r}$ with $m = 20$, $\gamma_R \equiv \dot{r}/r$, and $\gamma_\rho \equiv \dot{\rho}/\rho$).

The velocity and acceleration profiles of the aluminum/foam interface are shown in the second subplot in Fig. 2(b). With the 300 mg/cm^3 foam, the marker begins moving inwards at 60 μm/ns followed by a long period of interface deceleration from about 5 μm/ns^2 down to 1.5 μm/ns^2 before the rebounding shock hits the target. For the lower density 40 mg/cm^3 foam, the initial interface velocity is higher (75 μm/ns), and there is much less deceleration (1.6 μm/ns^2) over a shorter time period. However, the lower density foam has a larger Atwood number at the interface, $A_T = 0.8$ decreasing down to $A_T = 0.6$ before reshock, while the higher density foam has a nearly constant $A_T = 0.45$, seen in the third subplot of Fig. 2(b).

Epstein [*Phys. Plasmas* **11**, 5114 (2004)] derives a linear evolution equation for instability growth in a compressible cylindrical system:

$$\left(-\gamma_\rho + \frac{d}{dt}\right)\frac{d}{dt}\left(a_m \rho r\right) = \gamma_0^2 \left(a_m \rho r\right),$$

with $\gamma_\rho \equiv \dot{\rho}/\rho$ and $\gamma_0^2 \equiv (m/R)\, A_T \ddot{r}$, where $A_T = (\rho_2 - \rho_1)/(\rho_2 + \rho_1)$ is the Atwood number at the interface. Comparing γ_0, γ_ρ, and $\gamma_R \equiv \dot{r}/r$ allows one to crudely estimate the amount of growth expected to arise due to RT, compressibility, and convergence, respectively. With the 300 mg/cm^3 foam, the bulk of the growth arises from the γ_0 term (for $m = 20$), as can be seen in the bottom subplot of Fig. 2(b). However, when we use the lower density 40 mg/cm^3 foam, the γ_0 term is reduced, and the γ_R term is now comparable to it in magnitude. Thus, we expect more of the growth to be due to convergence (Bell-Plesset) effects with lower density foam, relative to our previous experiments. Note this is only a crude estimate based upon linear theory; more detailed analysis should be employed to further disentangle these effects.

3.2   2D Simulations

Using the as-metrologized dimensions from the inspection spreadsheet listed in Table 1, we ran preshot simulations for the three targets. These computations use LEOS and $\eta_{\text{laser}} = 0.75$, as these settings showed the best agreement for postshot simulations of the first shot day. Here, we use a pulse shape that is averaged over the three shots from our first shot day for the preshot simulations shown here. Recall that we run two sets of 2D computations for the cylinder implosions. The first is in a plane slice along the cylinder axis (r–z geometry), and the second is in a plane slice perpendicular to the cylinder axis (r–θ geometry). Synthetic radiographs are constructed by combining results from both sets.

Density plots at various times in the implosion for the r–z computation of the smooth target (DDD/S11) are shown in the left column of Fig. 3(a). Note that the shock rebounds from the axis just before 15 ns, and it is expected to hit the marker layer just after 17.5 ns. Here, we predict slightly more marker bowing than in the previous shot day. This is because we have tweaked the beam spot sizes that were fed in to `xRAGE` in order to more closely match what we believe is correct for the `NIF` elliptical beam spots. (A full discussion of the correct settings for the `xRAGE` laser package is beyond the scope of this document.)

Similar r–z computations for the perturbed targets (EEE/S12 and FFF/S13) were also run, and results for EEE and FFF are shown in the left column of Fig. 3(b) and (c), respectively. The shock appears slightly delayed relative to DDD, which we attribute to the slightly thicker ablator (near nominal 1479 μm outer radius for EEE and FFF, compared to 1465.8 μm outer radius for DDD). The jets at the axial ends of the aluminum marker here are attributed to the marker being much more recessed into the ablator region. In DDD, the inner ablator radius is 1287.9 μm, and the inner marker radius is at 1290.7 μm. However, in EEE the inner ablator radius is 1269.65 μm with the inner marker radius at 1289.6 μm (FFF is similar, but not quite as severe). A *caveat* is that the metrology measures the ablator inner radius at the axial end of the system ($z = 1500$ μm), not right next to the axial ends of the marker layer region ($z = \pm 400$ μm). If the CH ablator shrinks nonuniformly during the leaching, then the inner radius of the ablator might be closer to the inner radius of the aluminum near the axial ends of the marker. Thus, the jetting that `xRAGE` predicts might not be realized in the physical system.
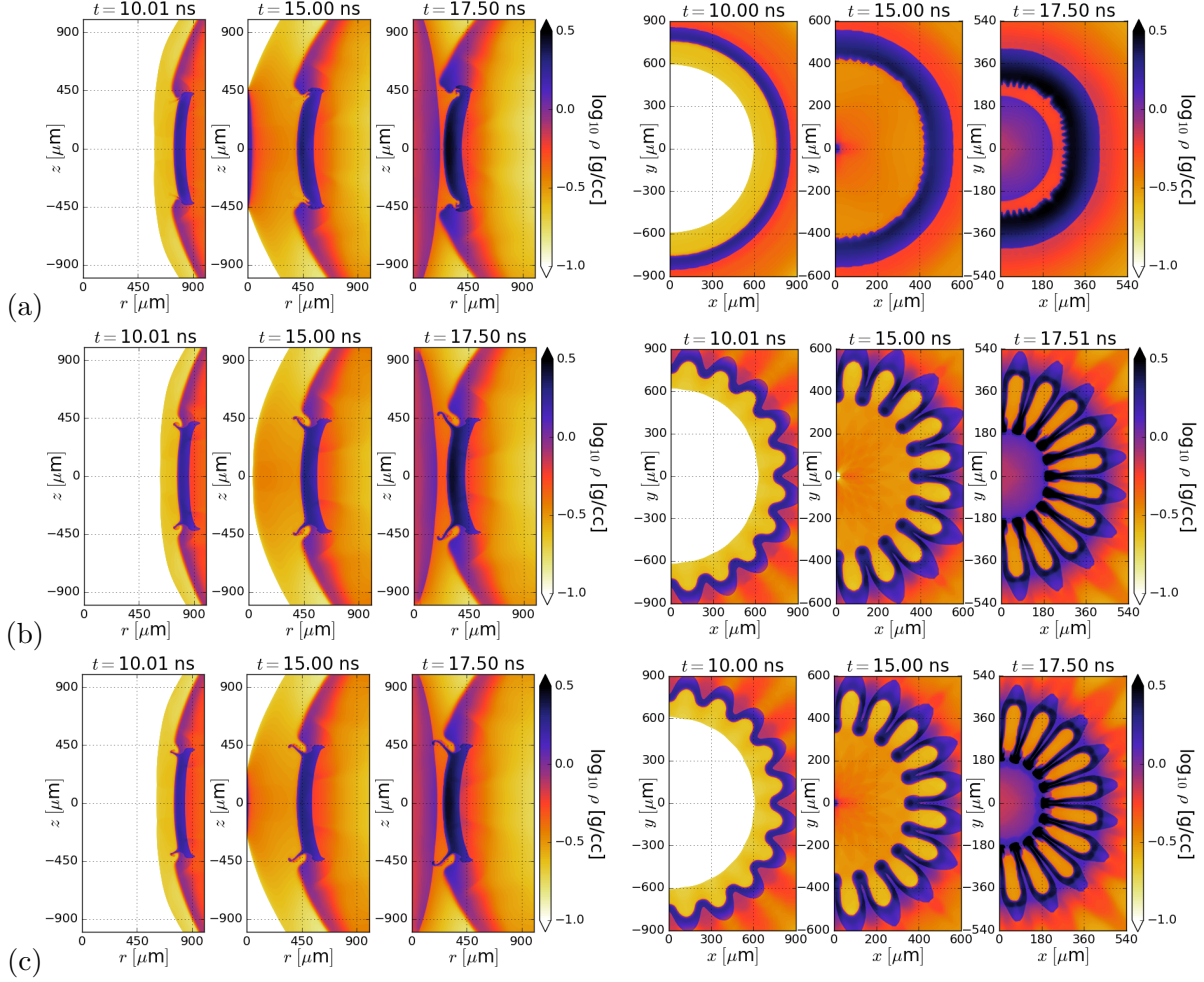
Figure 3: Log density at several times from r–z (left column) and r–θ (right column) preshot computations for (a) DDD (smooth target), (b) EEE (perturbed target), and (c) FFF (perturbed target).

Results from the r–θ computations of the three targets are shown in the right column of Fig. 3(a-c). Recall that for these r–θ calculations, we have tuned the laser drive such that the average (in θ) inner marker surface trajectory from a simulation with no initial perturbation matches the average (in z) inner marker surface trajectory from the corresponding r–z simulation. Because of this, and also because we do not expect to be able to accurately capture variations in the laser deposition profile in these 2D r–θ slices, these simulations all use an azimuthally symmetrized drive (laser deposition is smoothed over all θ). This has some implications for the discussion that follows.

First, we will examine results from the smooth target DDD on the right in Fig. 3(a). At early times, the marker appears largely circular, as it should with the azimuthally symmetrized drive. Further, the radial positions of the shock front and the marker are within a few μm from the r–z computations at these times. However, as the marker converges, it starts to square up along the coordinate axes. This is most notable at the last time $t = 17.5$ ns, but it is important to note that the azimuthally averaged $m = 0$ inner surface of the aluminum remains in good agreement with the axially averaged r–z results. This behavior is a fairly well-known phenomen in xRAGE, which is exacerbated in high convergence implosions. Even at the modest CR= 5 here, we are beginning to see this effect. It remains to be seen whether increasing the

8   LA-UR-20-xxxxx

maximum grid resolution (lower than the 2 μm used here), or using the un-split hydrodynamics advance, will help to alleviate this behavior.

This behavior is not nearly as evident in the two r–θ computations of the perturbed targets, EEE and FFF, shown in Fig. 3(b-c). Here, the large $m = 20$ sinusoidal perturbation dominates the evolution rather than the numerical effects seen in the smooth target. We start here with only the $m = 20$ mode using the initial amplitude measured by the touchprobe; other modes are not initialized here. At late times, the mushroom heads begin to develop on the spike tips, and evidence of Kelvin-Helmholtz roll-ups can be seen in the simulations when the rebounding shock hits the incoming spikes at $t = 17.5$ ns.

3.3   Synthetic Radiographs

We construct synthetic radiographs for the implosions by combining the two sets of 2D computations as described previously. A set of such synthetic radiographs are shown in Fig. 4. We have only included pinhole smearing here (by applying a 15 μm Gaussian smearing convolution), and the pinhole is assumed to be perfectly aligned with the cylinder axis for simplicity (no parallax). We do not include motion blurring in these images, as this would require simulation outputs at more frequent intervals than were used here.

Since the r–z geometry computations incorporate all of the effects of a smooth target, we can construct radiographs using only these results, as shown in Fig. 4(a) for DDD. There is no azimuthal variation present in these images, and the marker appears wider as a result of the finite amount of bowing. To include azimuthal variation, we replace the central 800 μm marker extent with results from a corresponding r–θ computation, as shown in Fig. 4(b). In this case, we now see some modest azimuthal variation, despite the fact that no large scale features are initially present. The small scale features come from numerical grid imprint, and we also see the larger $m = 4$ feature that was noted previously (squaring up of the circular cross-section). When the r–θ results are used over the finite axial extent of the marker, the aluminum region appears to get slightly narrower, due to the lack of any axial variation here, but the trajectories are in reasonable agreement to the r–z trajectories, differing by only a few μm.

Lastly, synthetic radiographs for one of the perturbed targets (EEE) is shown in Fig. 4(c). The evolution of the instability from early-time sinusoid through the development of the classic bubble and spike tips is evident, and at very late time we see mushroom heads forming on the spike tips. The rebounding shock strikes the spike tips around 17.5 ns. We expect to be able to image both the bubble and spike tip growth throughout the implosion for the perturbed targets.

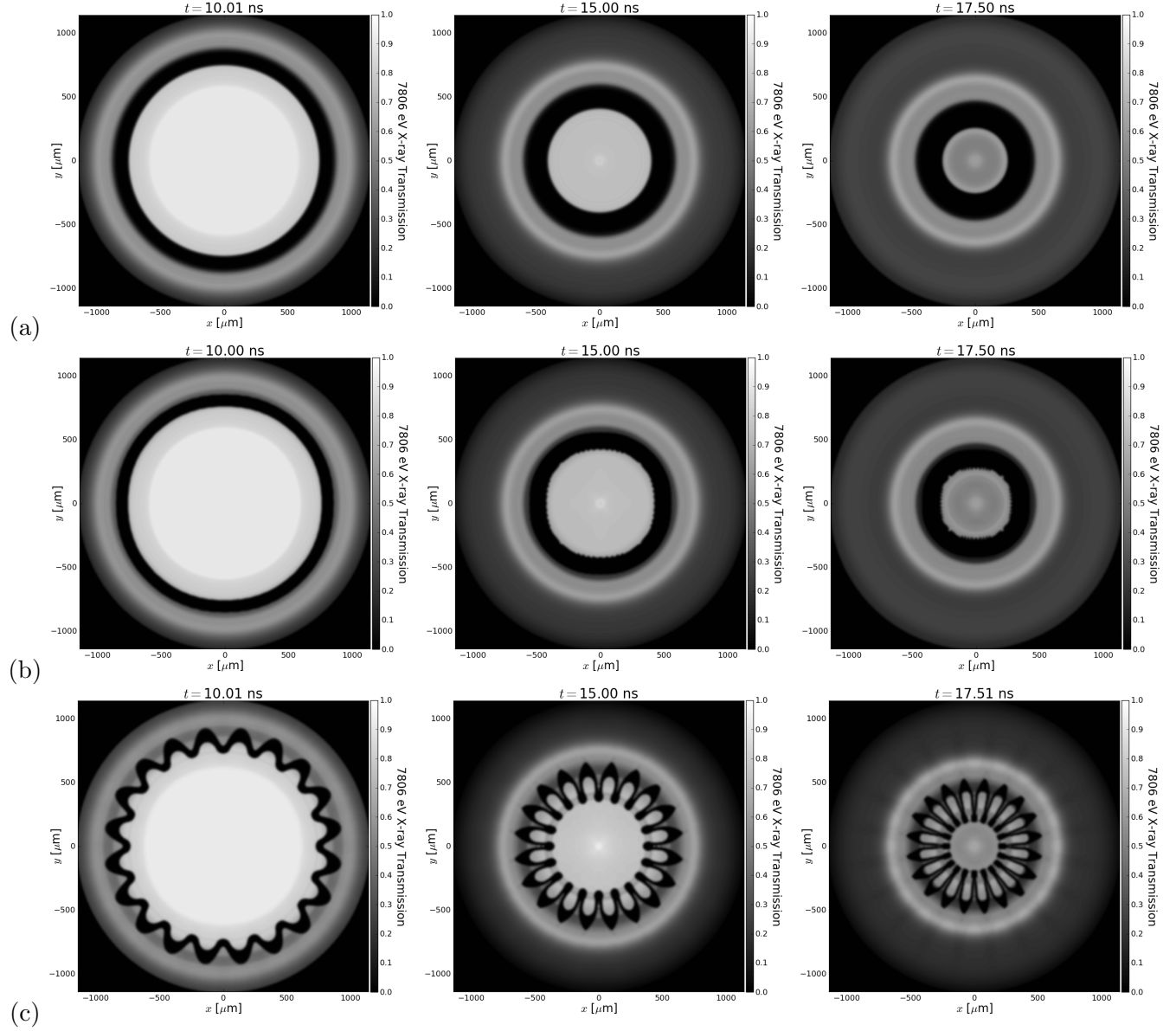Figure 4: Synthetic radiographs constructed from the preshot simulations. All images use 15 μm pinhole smearing, but no motion blurring is included here. (a) Results using only r–z geometry computation for DDD (smooth). (b) Results using both r–z and r–θ computations for DDD (smooth). (c) Results using both r–z and r–θ computations for EEE ($m = 20$) (results for FFF are similar).

4 Diagnostics

4.1 Primary

Our primary diagnostic is a pinhole framing camera in the polar DIM, 0-0, looking down the cylinder axis. This is a standard 4× pinhole framing camera. In the previous shot day, we used RGXD4-H-1000-12.7-4x, which has the pinhole plane offset 250 mm from target chamber center (TCC) and the image plane out another 1000 mm. For this shot day, we have switched to RGXD4-H-563-12.7-4x, with a pinhole standoff of 141 mm from TCC (image plane further out by roughly 563 mm). Timings for each shot are in Table 2.

We have also reduced the thickness of materials in the nosecap. Previously, we used 125 μm of Kapton on the TCC-side of the pinhole. This has been reduced to 25 μm. Similarly, in the kinematic base, we are now using only 6.25 μm of nickel (matching the backlighter material). We had previously used 25 μm of zinc (backlighter used on first shot day). Details are shown in the TaLIS slide reproduced here in Fig. 5. The effects of these changes on the expected photon counts are discussed in Sec. 4.3.
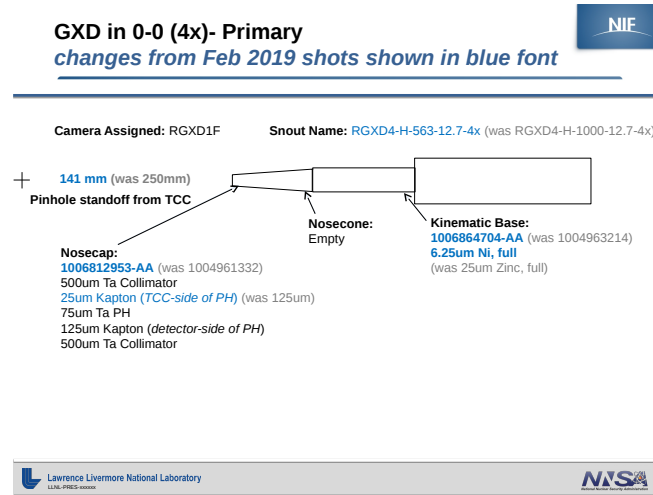

Figure 5: TaLIS slide for primary diagnostic.

4.2 Secondary

We have secondary diagnostics in two equatorial DIMs, 90-78 and 90-124. TaLIS slides for the secondary diagnostics are shown in Fig. 6. A 2× magnification gated pinhole framing camera is in 90-78 (RGXD4-H-836-25.4-2x, 418 mm pinhole standoff from TCC). On our first shot day, this imaged self-emission from the target during the drive phase onto a four-strip framing camera. Since the target does not evolve much during the drive, we have switched the timings of the last two strips back considerably. The third strip will now image around the time the shock is expected to coalesce on axis, and the fourth strip will image around the time the rebounding shock is expected to collide with the incoming aluminum marker. Timings are shown in Table 2. Preliminary estimates suggest we have little chance of seeing emission at these times though. At shock flash, the on-axis temperature peaks around 500–600 eV, while at shock rebound the aluminum gets to 100 eV.

The diagnostic in 90-124 is the time-integrated NIF X-ray Spectrometer (NXS). It is being fielded on only the first shot in order to gauge backlighter performance.
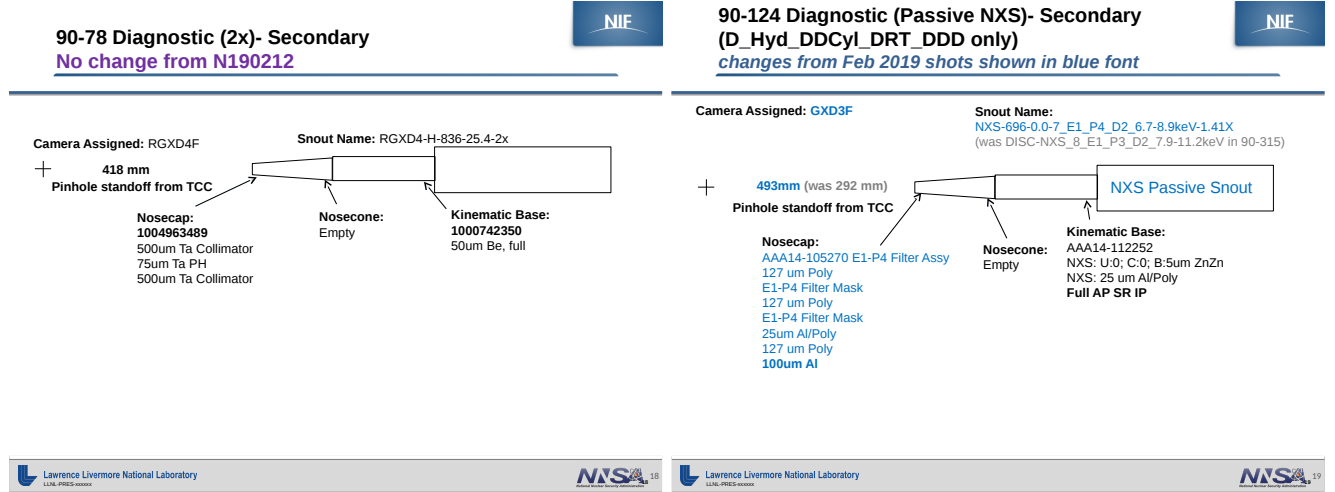
LA-UR-20-xxxxx

90-78 Diagnostic (2x)- Secondary
No change from N190212

NIF

Camera Assigned: RGXD4F

+ **418 mm**
Pinhole standoff from TCC

Snout Name: RGXD4-H-836-25.4-2x

Nosecap:
1004963489
500um Ta Collimator
75um Ta PH
500um Ta Collimator

Nosecone:
Empty

Kinematic Base:
1000742350
50um Be, full

Lawrence Livermore National Laboratory
LLNL-PRES-xxxxxx

NNSA 18

90-124 Diagnostic (Passive NXS)- Secondary
(D_Hyd_DDCyl_DRT_DDD only)
changes from Feb 2019 shots shown in blue font

NIF

Camera Assigned: **GXD3F**

Snout Name:
NXS-696-0.0-7_E1_P4_D2_6.7-8.9keV-1.41X
(was DISC-NXS_8_E1_P3_D2_7.9-11.2keV in 90-315)

+ **493mm** (was 292 mm)
Pinhole standoff from TCC

NXS Passive Snout

Nosecap:
AAA14-105270 E1-P4 Filter Assy
127 um Poly
E1-P4 Filter Mask
127 um Poly
E1-P4 Filter Mask
25um Al/Poly
127 um Poly
100um Al

Nosecone:
Empty

Kinematic Base:
AAA14-112252
NXS: U:0; C:0; B:5um ZnZn
NXS: 25 um Al/Poly
Full AP SR IP

Lawrence Livermore National Laboratory
LLNL-PRES-xxxxxx

NNSA 19

Figure 6: TaLIS slides for secondary diagnostics.

Table 2: Diagnostic timings for the `NIF` cylinders.

	S11 (DDD)	S12 (EEE)	S13 (FFF)
NIF Shot #			
NIF Target #	M-M0_0_36-04	M-M20_12_36-05	M-M20_12_36-06
Type	Smooth	Mode 20	Mode 20
GXD 0-0 Strip Times [ns]	13.6, 14.6, 15.6, 16.6	11.6, 12.6, 13.6, 14.6	14.6, 15.6, 16.6, 17.6
GXD 90-78 Strip Times [ns]	1, 3, 15, 18	1, 3, 15, 18	1, 3, 15, 18

4.3 Estimates of Photometrics (S. Palaniyappan)

Here, we include Sasikumar Palaniyappan's estimates of photometrics, accounting for all of the changes that were made for this upcoming shot day.

4.3.1 Effect of snout, source size, pinhole size and magnification

Last year we used a 4x snout (H-1000-12.7-4X) with conjugates of 250 mm and 1000 mm. The signals on the detector were ∼1000-2000. The background signal was ∼500. This time, we are using a different nose cone (H-563-12.7-4X) with conjugates of 141 mm and 563 mm. In both the shot days, we are using the same 15 μm pinhole and the same RGXD1F CCD camera. The calculation shows that we expect the signal on the CCD to increase by a factor of 5.

In `NIF` FY19A, $D_{sp1} = 250$ mm and $R_{s1} = 1.1$ mm.
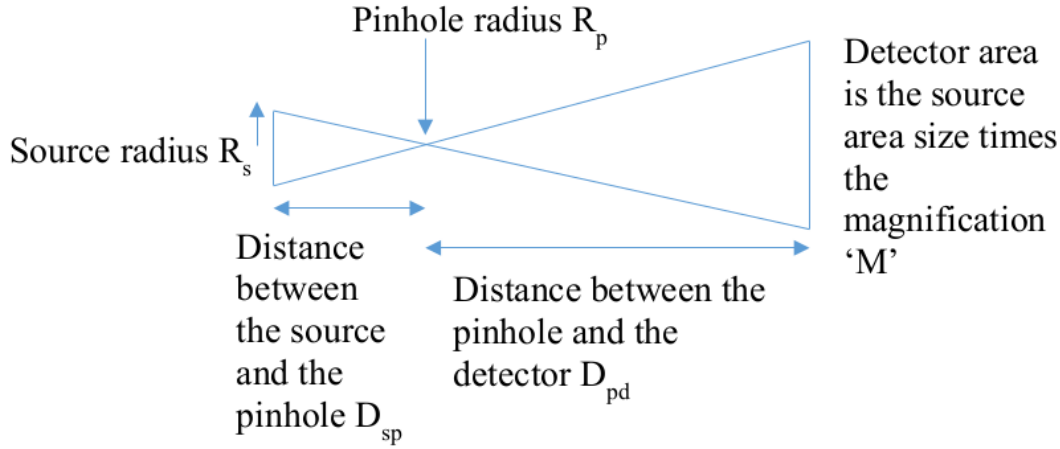
In `NIF` FY20A, $D_{sp2} = 141$ mm and $R_{s2} = 0.85$ mm.

In both shot days, the pinhole size is kept at 15um and the mag is also the same 4x.

Expected increase in signal $= \left(\frac{D_{sp1}R_{s1}}{D_{sp2}R_{s2}}\right)^2$.

Plugging the numbers give a factor of 5.3 increase in signal for FY20A compared to FY19A.

LA-UR-20-xxxxx

Sketch of the imaging configuration

Pinhole radius R_p

Detector area is the source area size times the magnification 'M'

Source radius R_s

Distance between the source and the pinhole D_{sp}

Distance between the pinhole and the detector D_{pd}

Let's say 'Y' is the # of x-ray photons at the source into 4π solid angle.

# of photons at the pinhole $= Y \times$ solid angle of the pinhole

$$= Y \ \frac{\pi R_p^2}{D_{sp}^2}$$

# of photons at the detector per unit area = # of photons at the pinhole/ Area of the detector

Area of the detector is mag 'M' times the area of the source $= M \times \pi R_s^2$

$\Rightarrow$ # of photons at the detector per unit area $= Y \ \dfrac{\pi R_p^2}{D_{sp}^2} \times \dfrac{1}{M \times \pi R_s^2}$

4.3.2 Effect of backlighter material and intensity/conversion efficiency changes

In `NIF` FY19A, we used Zinc backlighter with an intensity of 6×10^{14} W/cm^2. We used 32 BL beams at 0.7 TW/beam with BABLon7ns pulse shape and -18 mm focus offset to get to a spot size of 2.2 mm. For `NIF` FY20A, we are using Nickel backlighter with an intensity of 2×10^{15} W/cm^2. We use 32 BL beams with 1.4TW/beam and BABLon4ns pulse and zero focus offset.

Energy conversion to x-rays scales as $Z^{-3.5}$ to Z^{-4}.

Improvement: $(\text{Ni/Zn})^{-3.5} \rightarrow (28/30)^{-3.5} = 1.27$

The conversion efficiency (CE) as a function of intensity for an element, in this case Fe ($Z{=}26$), is

$$\text{CE} = 3.6\% \exp\left[-0.5\left[\log\left(I/2.24 \times 10^{15}\right)/0.945\right]^2\right]$$

The CE is multiplied by the total energy to get the energy emitted in K-Shell radiation.

Using the functional fit for CE, increasing the intensity by a factor of 3 changes the CE by 1.17. This assumes Fe with the higher intensity of 2.2×10^{15} W/cm^2 and the lower intensity being a factor of 3 less. Note that there is a specific intensity for peak CE that varies with Z. It is possible to overdrive the backlighter, reduce the CE, and potentially decrease the total energy in x-rays.

This rough scaling gives an increase in the number of photons in FY20 of 1.27 * 1.17 = 1.48 or a 48% increase compared to FY19A.
See: S. H. Batha, Cris W. Barnes, and C. R. Christensen, "Backlighter Predictive Capability," *Rev. Sci. Instr.* **74**, 2174 (2003).

4.3.3 Effect of 300 mg/cm^3 foam vs 30 mg/cm^3 and higher convergence implosion

`NIF` FY19A used 300 mg/cm^3 foam that is 5 mm long. The unshocked foam from 0–15 ns at 0.3 g/cm^3. The shocked foam density was ~1.5 g/cm^3 from 7 to 15 ns. The foam density increases from the shock and compression. From 15 ns to 20 ns, during the reshock, the foam density is ~5 g/cm^3.

FY19A (300 mg/cm^3 foam; Zinc BL)	Density [mg/cm^3]	Transmission [%]
Unshocked Foam (0–15 ns)	300	63.5
Shocked Foam (7–15 ns)	1500	10
Reshocked Foam	5000	0

`NIF` FY20A will use 30 mg/cm^3 foam that is 5 mm long. The unshocked foam from 0–11 ns at 0.03 g/cm^3 has a transmission of 94% for the Ni x-ray. The foam density was ~0.2 g/cm^3 from 5 to 11 ns. The foam density increases from the shock and compression. From 11 ns to 13.5 ns, during the reshock, the foam density is ~ 1 g/cm^3.

FY20A (30 mg/cm^3 foam; Nickel BL)	Density [mg/cm^3]	Transmission [%]
Unshocked Foam (0–15 ns)	30	94
Shocked Foam (7–15 ns)	200	64
Reshocked Foam	1000	11

The transmission through the un-shocked foam increases by a factor of 1.48 during FY20A compared to FY19A.

4.3.4 Effect of rear filter

FY19A used 25 μm Zinc filter. It has a transmission of 46% at 8.8 keV. Such thick filter was used to protect the CCD from debris as a very conservative approach due to massive W washer issues. FY20A will use 6.25 μm Nickel filter. It has a transmission of 75% at 7.8 keV.
We expect a factor of 1.63 increase in transmitted x-ray signal from FY19A to FY20A.

4.3.5 Combined effects

Adding all the effects together, we expect an increase of 5.3× (snout change), 1.5× (BL material and intensity changes), 1.5× (foam density and CR changes), and 1.63× (rear filter change) leading to an overall increase of ~ 19.5× **increase in signal for FY20A compared to FY19A.**

4.4 Analysis of Diagnostic Changes (B. Tobias)

Here, we include a detailed analysis by Ben Tobias regarding the changes made to the diagnostic setup.

4.4.1 Experimental design using algorithmic differentiation: pinhole imaging

For the upcoming `NIF CylDRT` experiment, Sasi has proposed to shorten up the pinhole camera geometry, without changing pinhole diameter, with the goal of improving signal. These analyses validate that choice, suggest that image resolution is probably not impacted at all, and serve as very simple demonstration of algorithmic differentiation as a component of experimental design.

Consider the task of optimizing a backlighter pinhole camera for detecting contrast features, such as the position of an imploding marker layer. The certainty with which the position of some feature, let's take it to be a spike or a bubble like we seek to diagnose in the cylindrical deceleration-phase R.-T. experiments, is predominantly a function of the signal-to-noise ratio (SNR) and the image blur (see other work pertaining to edge detection in MeV flash radiography). The goal is to maximize the signal, minimize the blur, or find some optimal compromise between the two. Here, I'm going to build a simple model for blur from the pinhole transfer function (PTF), another model for SNR, and show how algorithmic differentiation of the two provides guidance for experimental design. We'll work throughout this report in a parameter range relevant to 4x pinhole imaging with Ni backlighter at the NIF.

Pinhole transfer function (PTF):

This model is borrowed from [Benedetti 2017, Swing and Rooney 168]. The model equations depend on the x-ray energy, pinhole diameter, and radiographic conjugates. They provide a transfer function in the frequency space of the object being radiographed:

$$F = F_{ff}(\nu) \, Bessinc\left\{\pi d \left[1 + \frac{z_2}{z_1}\right] \nu F_{ff}(\nu)\right\}, \nu \leq \frac{d}{\lambda z_2}$$

$$F_{ff}(\nu) = \frac{2}{\pi}\left\{\arccos\left[\frac{\lambda z_2 \nu}{d}\right] - \frac{\lambda z_2 \nu}{d}\left[1 - \left(\frac{\lambda z_2 \nu}{d}\right)^2\right]^{\frac{1}{2}}\right\}$$

$$Bessinc(r) = \frac{J_1(r)}{r}$$

In Figure 7 I show the evaluation of this equation set for a few sample geometries. For now, I'm keeping the same nosecone, so as the pinhole is brought closer to the source magnification changes. As one expects, the smaller pinhole, close to the source, provides the best frequency response (least blur). As a figure of merit, I take the 50% point on these transfer functions: 67, 90, and 56 mm^{-1}, respectively.

Algorithmic differentiation:

The model above is written out in Python 3.7, and I've installed the open-source Autograd library to evaluate the differentials. Autograd executes a computational trace in the forward direction to determine dependencies amongst variables of the transform, then evaluates the local derivative of output variables as a function of independent input variables by multiplying intermediate differentials according to the chain rule. The intermediate differentials are taken from a library defining differential functions for each operation in the forward primal trace.

I've chosen the 50% PTF frequency to be the dependent variable (metric to be maximized in experimental optimization), and the independent variables are pinhole diameter and source-pinhole distance (again, pinhole-detector distance is fixed thus far).
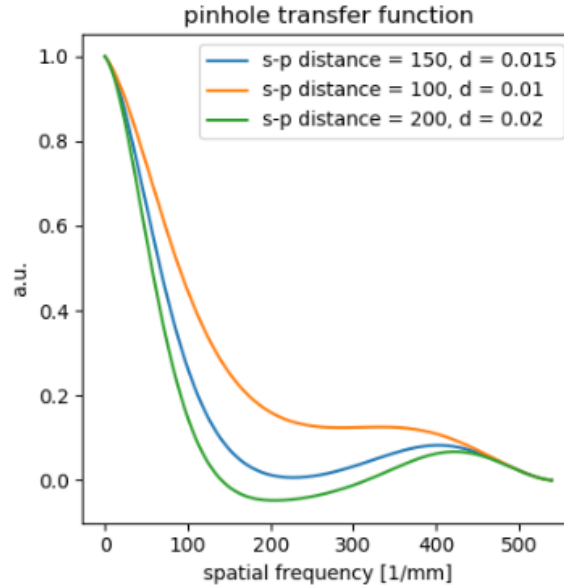
Figure 7: The change in pinhole transfer function vs. the distance from the pinhole to the backlighter source and pinhole diameter (both mm). The nosecone is assumed to be fixed, so the magnification is changing in each case, too. The small pinhole close to the source provides the best resolution (broadest transfer function).

Autograd does not have library entries for all the required special functions, so some modifications of the original forward transformation code had to be adopted:

1– There is no library entry for `scipy.special.cv` (Bessel functions of the first kind). A few new lines of code provide an equivalent but differentiable function for which each constituent operation has an Autograd library entry:

```
def jv( x ):
  phi = np.outer(np.ones(np.size(x)),np.linspace(0,np.pi,200))
  return 1/199*np.sum(np.cos(phi-np.outer(x,np.sin(phi[0,:]))),axis=1)
```

2– There is no library entry for `numpy.trapz`, so again it has to be re-defined locally:

```
def trapz(y, x):
  d = np.diff(x)
  return np.sum((y[0:-1] + y[1:]) * d / 2)
```

3– Finding the 50% point would have been most easily accomplished using a root-finding command. However, differentiation of an optimizer is, well, circular logic. Instead, I approximate the root with the following algorithm:

```
def Fresp(params):
  nu, f = PTF(params)
  fhalf = (f - 0.5)**2 * 1E6 + nu
  root = np.amin(fhalf)
  return root
```

The array min and array max functions amount in some sense to control flow routines, and so there is no conflict with Autograd differentiation, it's simply manipulating the original PTF such that a minimum corresponds with the value I wish to obtain. Differentiation of the top-level function is now simply two lines of code:

```
from autograd import value_and_grad

f=value_and_grad(Fresp)
jacobian = f(params0)[1]
```

A normalized Jacobian about the design point is defined in the following way:

$$J_{i,j} = \frac{\partial y_j}{\partial x_i} \times \frac{x_i}{y_j}$$
$$\bar{J} = J/|J|$$

For the frequency response as a function of s-p distance and pinhole diameter, the result is $[0.76635238, 0.64242045]$. Frequency response improves as one moves further away from the source (in this case also reducing magnification), and is inversely proportional to pinhole diameter. By moving in the direction $x \times \left[[0.766^{-1}, 0.642^{-1}]\right]$, one can expect to hold the 50% frequency response point approximately constant. This is shown in Figure 8:
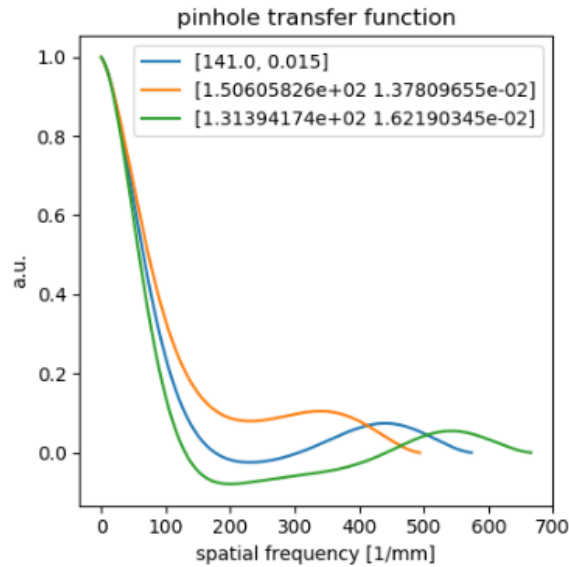

Figure 8: By changing parameters in a direction implied by the local gradient, the 50% frequency response point is held nearly constant. Differences are due to the minimum gradient direction changing over the scale of the step size. Also, the tails of the PTF and ringing features are ignored in our metric, so they're not part of the comparison even though they would impact image formation.

Signal to noise ratio (SNR):

Relative change in SNR is approximated in a very simple way by holding backlighter power fixed, calculating the solid angle subtended by the pinhole, and reducing photon intensity at the detector by a factor of the magnification. Relative SNR is then simply the square root of the relative intensity. Because

the nosecone dimension (p-d distance) is fixed, the area of the source must change. In practice this would complicate things significantly since conversion efficiency depends on intensity, but this exercise is just illustrative so it's ignored here. The problem goes away when one fixes the magnification and allows for re-design of the nosecone.

For a fixed p-d distance, the gradient in SNR w.r.t. s-p distance and pinhole diameter is [0.4472136, 0.89442719]. This vector points into a different quadrant than that for frequency response, but is NOT parallel to it. This implies that it's possible to at least hold one figure of merit constant while improving the other. In fact, because they are also not perpendicular, there exist a finite range of directions that improve both simultaneously!

Optimization of experimental design:

It is not always possible to do so, but because we only have 2 independent variables in this simple model, we can show each of the design merits as a surface plot. Figure 9 shows both, along with the product of the two. (Performance is not so simple as multiplying resolution by SNR, but here it's illustrative.)
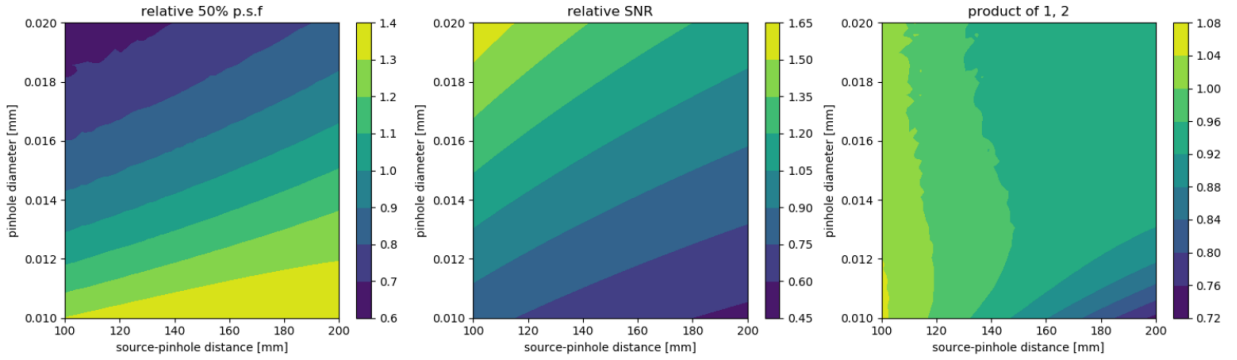

Figure 9: Contour plots of relative 50% PTF and SNR vs. the independent parameters of the experiment. Note that the contours in the first 2 sub-plots do not line up, meaning that one can hold performance constant in one respect while improving performance in the other. If overall performance were simply the product of resolution and noise, then the third sub-plot would guide optimization of the design space.

The data in Figure 9 is obtained by keeping the same nosecone and moving the pinhole closer or further from the source. These contours in the first and second panels are both more or less linear, so they provide a good example as to how optimization of resolution could be performed while holding SNR constant. One would simply follow a contour in the middle plot from top right to bottom left to maintain signal. These contours cross those in the first panel in a positive sense, improving the PTF. As noted earlier, changing the s-p distance changes the magnification, so it would also change the intensity on the backlighter and resulting conversion efficiency. Therefore, this is an inadequate model for those constraints. It's moot when magnification is fixed. Figure 10 shows the same type of data as Figure 9, but for fixed magnification:

Now that magnification is fixed, the contours in the first panel are more or less horizontal in regions of interest (small pinholes at a great distance produce rather messy PTFs with narrow first diffraction lobes). The SNR contours are straight lines. In fact, around the current design point (141 mm s-p, 0.015 mm pinhole), the normalized Jacobian is $\left[\sqrt{\frac{1}{2}}, \ \sqrt{\frac{1}{2}}\right]$. Although this could have been arrived at analytically without much effort, the complicated nature of PTF would have been daunting to address quantitatively.
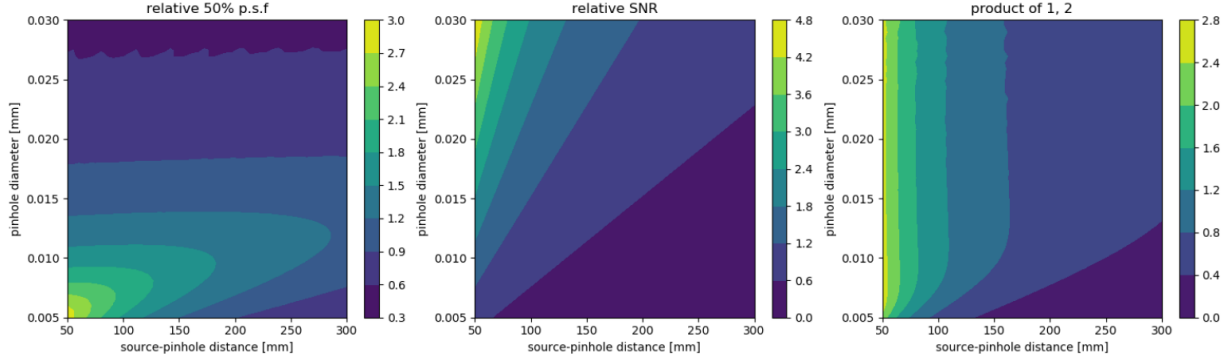
Figure 10: Same as Figure 9, but magnification is fixed. The p-d distance is not shown here, but assumed to be 4× the s-p distance. A larger range of conjugate distances are considered since NIF nosecones range from roughly 550 to 1000 mm in length.

Still to do:

The next steps here would be to define a single figure of merit that represented resolving power in terms of SNR and blur, as was done for other radiography studies. That cost function could be minimized through constrained, gradient-driven optimization. There are elements and considerations missing here, some of them could be introduced to the optimizer as constraints or weights, and some of them would be integral to the blur and SNR models. Nonetheless, some value has already been provided by this simple formulation:

1. The estimates validate Sasi's decision to go with a shorter nosecone in FY20 at the NIF. This should improve signal quite a bit without sacrificing spatial resolution.

2. Sasi probably could have gone to a 10 μm pinhole as well, without *losing* signal (in comparison to FY19). This would have improved pinhole resolution by something like 75%, whereas the current choice is a 40–50% improvement in SNR.

3. As can be inferred from the third panel in Figure 9, now that the nosecone is fixed, a slight change in magnification can have a beneficial impact on SNR, but at the cost of blur. Conversely, changing the pinhole at this point will reduce SNR about as much as it improves blur. The impact of this tradeoff on overall performance of the imager isn't as simple as that implies, but it suggests one is justified in sticking with the 15 μm pinhole for now. SNR was a big problem in FY19, it's not obvious that pinhole blur dominated the image.

Point 3 above suggests another element that should be folded in, namely the detector MTF. Given that the detector point spread function has a Gaussian with of 50–60 μm, detector blur is almost certainly dominating over pinhole blur for this particular experiment. Working at a magnification of 12, for example, the situation would be somewhat different.

The Autograd element here is providing limited value given that we have very few independent parameters. Figures 9 and 10 are obtained by sampling the design space brute-force, and that data yields insight more readily. Differentiation techniques will truly shine in cases where there are many independent design parameters that have to be weighed against each other, evaluated for trade-offs, and simultaneously optimized. In those cases, gradient information will make the job much easier than finite-differencing or Monte Carlo searching, so this simple and easy to follow example is just good practice for bigger jobs on the horizon.